

MicroRNA silencing for cancer therapy targeted to the tumour microenvironment

Christopher J. Cheng^{1,2,3,†}, Raman Bahal⁴, Imran A. Babar^{1,†}, Zachary Pincus^{1,†}, Francisco Barrera^{3,†}, Connie Liu¹, Alexander Svoronos³, Demetrios T. Braddock⁵, Peter M. Glazer⁴, Donald M. Engelman³, W. Mark Saltzman² & Frank J. Slack^{1,†}

MicroRNAs are short non-coding RNAs expressed in different tissue and cell types that suppress the expression of target genes. As such, microRNAs are critical cogs in numerous biological processes^{1,2}, and dysregulated microRNA expression is correlated with many human diseases. Certain microRNAs, called oncomiRs, play a causal role in the onset and maintenance of cancer when overexpressed. Tumours that depend on these microRNAs are said to display oncomiR addiction^{3–5}. Some of the most effective anticancer therapies target oncogenes such as *EGFR* and *HER2*; similarly, inhibition of oncomiRs using antisense oligomers (that is, antimiRs) is an evolving therapeutic strategy^{6,7}. However, the *in vivo* efficacy of current antimiR technologies is hindered by physiological and cellular barriers to delivery into targeted cells⁸. Here we introduce a novel antimiR delivery platform that targets the acidic tumour microenvironment, evades systemic clearance by the liver, and facilitates cell entry via a non-endocytic pathway. We find that the attachment of peptide nucleic acid antimiRs to a peptide with a low pH-induced transmembrane structure (pHLIP) produces a novel construct that could target the tumour microenvironment, transport antimiRs across plasma membranes under acidic conditions such as those found in solid tumours (pH approximately 6), and effectively inhibit the miR-155 oncomiR in a mouse model of lymphoma. This study introduces a new model for using antimiRs as anti-cancer drugs, which can have broad impacts on the field of targeted drug delivery.

Silencing aberrantly expressed microRNAs (miRNAs) *in vivo* has been achieved using antisense with various nucleic acid analogues involving locked nucleic acids (LNAs), 2'-O-methyl oligonucleotides (for example, antagomiRs), and peptide nucleic acids (PNAs) or nanoencapsulated PNAs^{5,9,10}. As with most RNA-based therapies, each of these strategies is stymied by non-specific organ biodistribution, reticuloendothelial system clearance, and endolysosomal trafficking^{8,11}. Acidosis is a hallmark of tumours¹². The pHLIP peptide forms an inducible transmembrane α -helix under acidic conditions¹³, has the ability to translocate membrane-impermeable molecules into cells via a non-endocytic route^{13,14}, and, when administered systemically, can target a variety of epithelial tumours¹⁵. Exploiting acidity as a general property of the tumour microenvironment, we find that the pHLIP peptide can localize to tumours of lymphoid origin in a subcutaneous flank model (Fig. 1a) and a model of disseminated lymphadenopathy (Fig. 1b), while avoiding the liver. Although pHLIP also shows kidney targeting, much of the peptide is cleared by renal excretion (Extended Data Fig. 1). To exploit these targeting and delivery properties we developed a tumour-targeted antimiR delivery vector (pHLIP-antimiR).

PNAs are nucleic acid analogues comprising nucleobases joined by intramolecular amide bonds. This backbone imparts stability, nuclease resistance, and an increased binding affinity for complementary nucleic acids¹⁶. We hypothesized that pHLIP would facilitate the intracellular delivery of charge-neutral PNA antimiRs (Fig. 1c), which lack anionic

phosphodiester groups, to cells within the tumour microenvironment. Tethering PNA antimiRs to pHLIP represents a unique approach because the multifunctional peptide component both targets tumours and mediates lipid membrane translocation¹³.

Fabrication of pHLIP-antimiR was verified by reversed-phase high-performance liquid chromatography (RP-HPLC), tricine SDS-polyacrylamide gel electrophoresis (SDS-PAGE), electrophoretic mobility shift assay (EMSA), and mass spectrometry (Extended Data Fig. 2a–c). In our constructs, the linkage between the PNA and peptide comprised a disulphide bond, which can be cleaved in the reducing environment of the cytosol (Fig. 1c)¹⁷; therefore, attachment to the inserting carboxy (C) terminus of pHLIP promotes the intracellular delivery of the PNA antimiR. When administered to A549 cells (Fig. 2a and Extended Data Fig. 2d) and Toledo diffuse large-B cell lymphoma (DLBCL) cells (Extended Data Fig. 2e, f), which express elevated levels of miR-155 compared with other DLBCL cells¹⁸, a pHLIP-antimiR modified with a 5-carboxytetramethylrhodamine (TAMRA) label attached to the PNA resulted in enhanced cellular delivery at acidic extracellular pH compared with neutral pH. PNA delivery to cells by pHLIP does not appear to be greatly affected by sequence since antimiR uptake has been demonstrated with numerous miRNAs including miR-182 (Fig. 2a and Extended Data Fig. 2d), miR-155 (Extended Data Fig. 2e, f), scrambled miR-155, miR-21, and

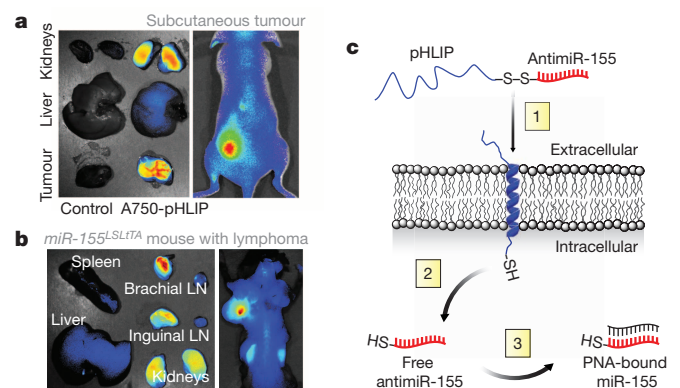


Figure 1 | Targeting miR-155-addicted lymphoma using pHLIP.

a, b, Targeting distribution of pHLIP labelled with Alexa Fluor 750 (A750-pHLIP) 36 h after systemic administration to **(a)** a nude mouse with miR-155 flank tumours ($n = 3$) and **(b)** a *mir-155^{LSL1TA}* mouse with lymphadenopathy ($n = 3$); Alexa Fluor 750 conjugated to cysteine was the control. LN, lymph nodes. **c**, Schematic of pHLIP-mediated PNA antimiR delivery. (1) At pH less than 7, the C terminus of pHLIP inserts across lipid bilayers, which facilitates delivery of attached antimiR-155. (2) The disulphide between pHLIP and antimiR-155 is reduced in the cytosol. (3) Intracellular antimiR-155 is free to inhibit miR-155.

¹Department of Molecular, Cellular and Developmental Biology, Yale University, New Haven, Connecticut 06511, USA. ²Department of Biomedical Engineering, Yale University, New Haven, Connecticut 06511, USA. ³Department of Molecular Biophysics and Biochemistry, Yale University, New Haven, Connecticut 06511, USA. ⁴Department of Therapeutic Radiology, Yale University, New Haven, Connecticut 06511, USA. ⁵Department of Pathology, Yale University, New Haven, Connecticut 06511, USA. [†]Present addresses: Alexion Pharmaceuticals, Inc., 352 Knott Drive, Cheshire, Connecticut 06410, USA (C.J.C.); OrbiMed Advisors LLC, 601 Lexington Avenue, 54th Floor, New York, New York 10022, USA (I.A.B.); Departments of Developmental Biology and Genetics, Washington University, St. Louis, Missouri 63110, USA (Z.P.); Department of Biochemistry and Cellular and Molecular Biology, University of Tennessee–Knoxville, Knoxville, Tennessee 37996, USA (F.B.); Department of Pathology, Beth Israel Deaconess Medical Center, 330 Brookline Avenue, Boston, Massachusetts 02215, USA (F.J.S.).

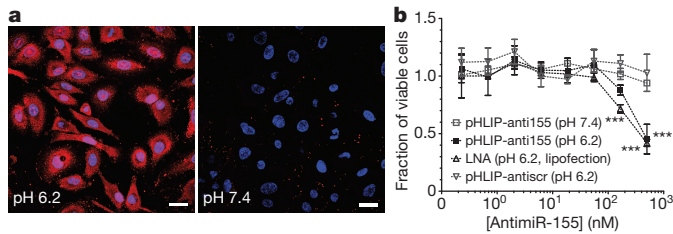


Figure 2 | Intracellular translocation of PNA anti-miRs mediated by pHLIP. **a**, Confocal projections of A549 cells incubated with labelled pHLIP-anti-miR (against control miR-182); scale bars, 25 μm . Red, PNA-TAMRA; blue, nucleus. **b**, Effects of miR-155 inhibition on KB cell viability; all data are normalized to cells treated with vehicle buffer. Data are shown as mean \pm s.d., with $n = 3$; statistical analysis performed with two-way analysis of variance (ANOVA); *** $P < 0.001$.

miR-210. Delivery of anti-miR-155 by pHLIP (pHLIP-anti155) depressed luciferase in miR-155-overexpressing¹⁹ KB cells that stably expressed a miR-155-targeted dual luciferase sensor (Extended Data Fig. 2g). Additionally, inhibition of miR-155 by pHLIP-anti155 reduced KB cell viability at a dose comparable to LNA (15-base oligonucleotide, Exiqon) anti-miR-155 delivered by lipofection (Fig. 2b). To demonstrate the adaptability of this anti-miR delivery technology to silencing other miRNAs, pHLIP was attached to a PNA anti-miR against miR-21, which de-repressed a miR-21 luciferase sensor (Extended Data Fig. 2h). Together, these data suggest that pHLIP-anti-miR is effective at delivering PNA anti-miRs to multiple cancer cell types, in which endocytosis is hypothesized to be relegated to a supplementary mode of cell uptake due to the transport properties of pHLIP.

Certain oncomiRs have emerged as pharmacological targets. For example, ectopic expression of miR-155 in mice provided the first evidence that dysregulation of a single miRNA could cause cancer²⁰. Although aberrant expression of miR-155 is characteristic of numerous cancers, miR-155 is notorious for its oncogenic involvement in lymphomas²¹. We previously developed a Tet-Off-based mouse model in which miR-155 expression is induced in haematological tissues and can be attenuated with the addition of doxycycline (DOX)⁵. Between 2 and 3 months of age, these *mir-155*^{LSLIT4} mice develop disseminated lymphoma, in which lymphoid tissues progress from normal histology, to follicular hyperplasia, to follicular lymphoma, to DLBCL (Extended Data Fig. 3a, b). Although these are aggressive cancers comprising neoplastic B cells with a high Ki-67 proliferative index, the disease dramatically regresses upon DOX-induced miR-155 withdrawal (Extended Data Fig. 3b, c). Therefore, this is a model of oncomiR addiction in which tumorigenesis is dependent on expression of miR-155 and its removal leads to cancer regression²².

We assessed the therapeutic efficacy of pHLIP-anti155 *in vivo* using two tumour models based on *mir-155*^{LSLIT4} mice: (1) nude mice subcutaneously implanted with neoplastic B cells derived from the enlarged spleens of *mir-155*^{LSLIT4} mice (Extended Data Fig. 4a) and (2) *mir-155*^{LSLIT4} mice after progression to conspicuous lymphadenopathy (Extended Data Fig. 4b). Continuous suppression of miR-155 via DOX-impregnated mouse chow or a cocktail of chemotherapeutics and anti-inflammatory steroids (CHOP) served as positive controls that each caused tumour regression (Extended Data Fig. 5a). Since CHOP is part of the current standard of care for human lymphomas²³, the similar response to treatment with DOX and CHOP demonstrated the potential utility of anti-miR-155 cancer therapy. Accordingly, intravenous administration of pHLIP-anti155 to the flank tumour model resulted in a significant reduction in tumour growth (Fig. 3a). In a subsequent study at a higher dose, pHLIP-anti155 showed a significant survival advantage compared with a commercially available LNA (Exiqon) anti-miR optimized for *in vivo* miR-155 silencing (Fig. 3b and Extended Data Fig. 5b). After administration of pHLIP-anti155, mice exhibited no clinical signs of distress, toxicity, and renal damage (Extended Data Fig. 5c). Note that the dose of pHLIP-anti155 used in this study was much lower (ranging from 17- to 40-fold) than that used in other anti-miR delivery reports^{10,24}.

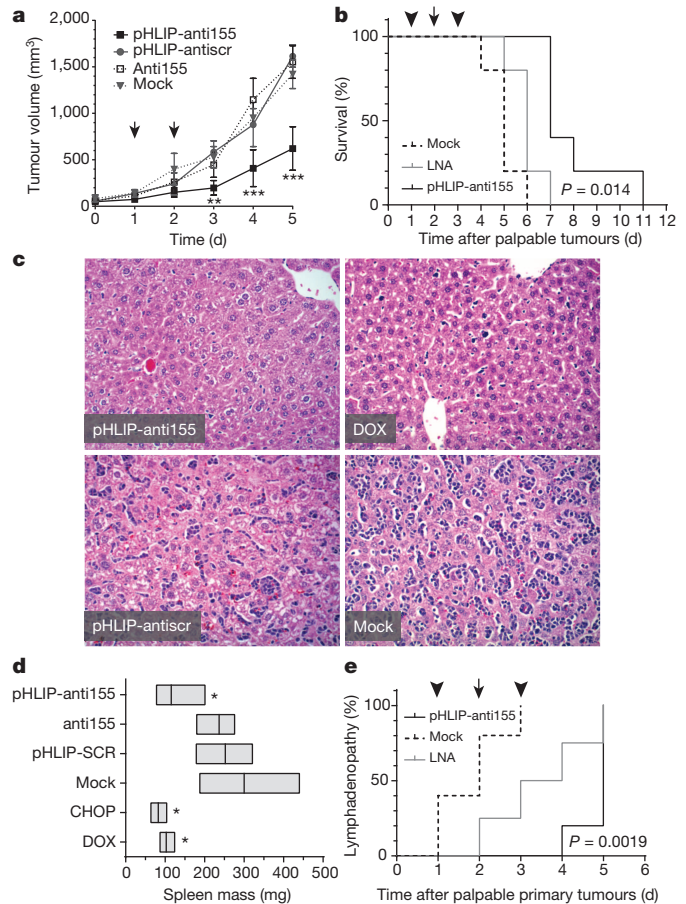


Figure 3 | Targeted silencing of miR-155 has beneficial effects in mice with subcutaneous *mir-155*^{LSLIT4} tumours. **a**, Tumour growth response to treatment; arrows represent 1 mg kg⁻¹ PNA dose per intravenous injection; all with $n = 3$, except for pHLIP-anti155 group with $n = 4$. **b**, Survival in response to anti-miR treatment; cutoff criteria include tumour volume greater than 1 cm³ or clinically mandated euthanasia. Symbols represent 2 (arrowhead) or 1 (arrow) mg kg⁻¹ intravenous injections; LNA is a fully phosphorothioated LNA anti-miR against miR-155; $n = 4$ for all groups; (*) for pHLIP-anti155 compared with LNA. **c**, Representative histological analysis of livers (haematoxylin and eosin (H&E), $\times 200$ magnification) harvested from early endpoint study (Fig. 3a and Extended Data Fig. 5a). **d**, Mass range of spleens from mice in early endpoint study; all with $n = 3$, except for pHLIP-anti155 group with $n = 4$. **e**, Time to development of conspicuous lymphadenopathy in survival study; (**) for pHLIP-anti155 compared with mock. Data are shown as mean \pm s.d.; statistical analysis performed with (a) two-way ANOVA, (b, e) Mantel-Cox test, or (d) two-tailed Student's *t*-test; * $P < 0.05$; ** $P < 0.01$; *** $P < 0.001$.

In addition to delaying tumour growth, pHLIP-anti155 treatment suppressed the metastatic spread of neoplastic lymphocytes to other organs. The liver, lymph nodes, and spleen were common targets for metastatic lymphocytes. In a blinded pathological assessment, livers from mice treated with pHLIP-anti155 and DOX had rare scattered aggregates of one to three neoplastic lymphocytes, while livers in the negative control groups typically had dense tumoral aggregates of up to two dozen cells scattered throughout the entire organ (Fig. 3c)—note that these tissues were harvested at an early endpoint (that is, when the negative controls reached a tumour size of 1 cm³, Fig. 3a) in relation to the survival study (Fig. 3b) to resolve pharmacological effects. Early endpoint treatment with pHLIP-anti155, DOX, and CHOP reduced the onset of splenomegaly (as judged by spleen mass), which occurred in all of the negative control groups (Fig. 3d). Additionally, pHLIP-anti155 significantly delayed the development of conspicuous lymphadenopathy (Fig. 3e), which was particularly evident in the inguinal and axillary lymph nodes throughout all of the organs (Extended Data Fig. 5d).

On the basis of a blinded complete blood count analysis, the negative control groups comprised a large number of atypical mononuclear cells of lymphoid origin—consistent with the leukaemic phase of lymphoma. Treatment with pHLIP-anti155 and DOX had levels of circulating lymphocytes similar to wild type, while CHOP treatment resulted in lymphocyte levels much lower than wild type (Extended Data Fig. 5e). Although pHLIP can target to metastasized lymph node tumours (Extended Data Fig. 1c), the therapeutic effects on the levels of circulating lymphocytes suggest that the lower incidence of metastatic spread is probably due to antimiR activity at the primary tumour. These findings support the effective targeting of systemic antimiR-155 therapy to neoplastic cells (Extended Data Fig. 5f). The additional lymphopenia caused by CHOP treatment probably reflects the general toxicity of nontargeted conventional chemotherapy drugs (Extended Data Fig. 5e). The absence of systemic toxicity may represent an important advantage for pHLIP-targeted antimiR therapy. Importantly, when healthy C57BL/6 mice were treated at the highest dose and frequency used in this study, pHLIP-anti155 showed no significant impairment of liver and kidney function (Extended Data Fig. 6a). Additionally, white blood cell levels (Extended Data Fig. 6b), body mass (Extended Data Fig. 6c), and organ mass (Extended Data Fig. 6d) were all within normal ranges.

In addition to the miR-155-addicted lymphoma subcutaneous tumour model, pHLIP-anti155 was also effective at treating KB cell xenograft tumours, which stably expressed luciferase for intravital monitoring of tumour bioluminescence (Extended Data Fig. 7), as well as disseminated tumours in *mir-155^{LSLTA}* mice. Although implanted subcutaneous tumour models are effective for evaluating tumour growth, spontaneous cancer models arising in endogenous tissues are a more clinically relevant means of assessing therapeutic efficacy. Remarkably, systemically administered pHLIP-anti155 accumulated in the enlarged lymph nodes of the transgenic *mir-155^{LSLTA}* mice (Fig. 4a). Furthermore, like most therapeutics, PNA oligomers are known to be cleared by the reticuloendothelial system¹¹, which results in accumulation in the liver; pHLIP-anti155 showed approximately 10-fold reduction in liver accumulation compared with anti155 alone (Fig. 4a and Extended Data Fig. 8a, b). The therapeutic impact of pHLIP-anti155 in *mir-155^{LSLTA}* mice was

supported by a statistically significant decrease in spleen size and a non-statistically significant reduction in lymph node tumour burden (Fig. 4b and Extended Data Fig. 8c–e). A non-statistically significant increase in apoptosis was also observed in the lymph nodes of treated mice (Extended Data Fig. 8f, g). Interestingly, blinded histopathological analysis revealed that spleens in pHLIP-anti155-treated *mir-155^{LSLTA}* mice had differentiated red and white pulp (similar to wild-type mice with no treatment), while the splenic architecture of *mir-155^{LSLTA}* mice treated with pHLIP-antisense was almost completely effaced (Fig. 4c and Extended Data Fig. 8h). As with the subcutaneous tumour studies, pHLIP-anti155 treatment also showed a 12-fold reduction in liver metastasis (Fig. 4d and Extended Data Fig. 8i, j), while flow cytometric analysis revealed reductions in populations of B220-expressing spleen cells (Extended Data Fig. 8k). Consistent with a lack of systemic toxicity, treatment with pHLIP-anti155 produced no histopathological kidney damage (Extended Data Fig. 8l). Lastly, all mice that developed lymphoma-induced paresis showed improved motor skills after pHLIP-anti155 treatment (Supplementary Videos 1–4, $n = 3$).

For a more direct assessment of miR-155 silencing in *mir-155^{LSLTA}* mice, we monitored the levels of miR-155 targets in response to antimiR treatment. As an oncogene in lymphoma, miR-155 suppresses genes involved in processes such as apoptosis, proliferation, immune response regulation, as well as cell differentiation and development²¹. However, the addition mechanisms by which lymphoma regresses upon miR-155 withdrawal are unknown. Typically, miR-155 targets have been identified by differential gene expression analysis of an overexpression condition compared with wild type²⁵. To uncover the genes required for miR-155 addiction, we performed RNA sequencing (RNA-seq) analysis on miR-155-addicted lymphoid tumours compared with regressing tumours (Extended Data Fig. 9a). This is the first study, to our knowledge, to identify miRNA cancer targets that directly result from oncomiR withdrawal. Out of 29,209 mouse genes, 2,101 showed significant upregulation or downregulation in response to miR-155 attenuation (Extended Data Fig. 9b and Supplementary Table 1). Kyoto Encyclopedia of Genes and Genomes (KEGG) analysis of upregulated genes revealed that 41% have been associated with cancer pathways (Extended Data Fig. 9c). Additionally, 25% have been implicated in cell adhesion and migration pathways

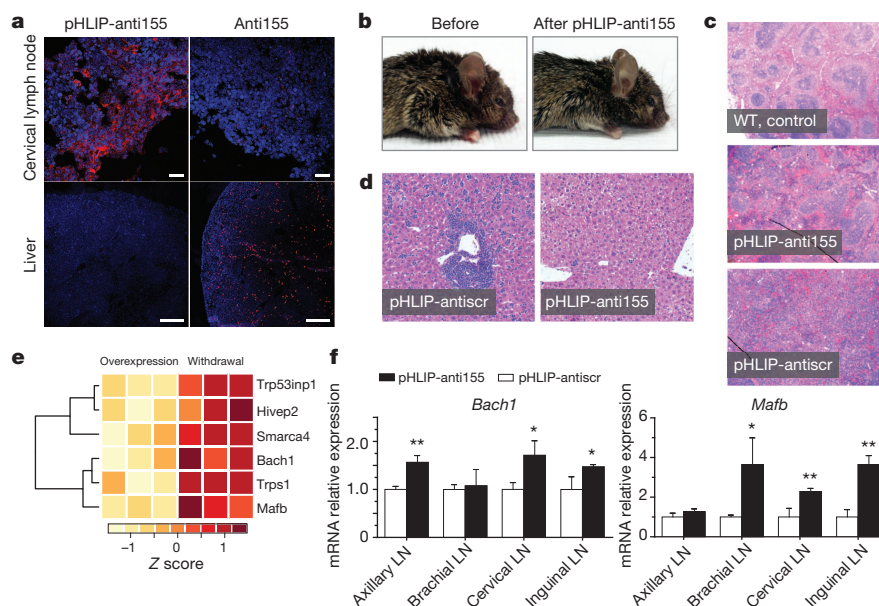


Figure 4 | Delivery of pHLIP-anti155 to *mir-155^{LSLTA}* mice with lymphadenopathy. **a**, Confocal projections of systemic, tumour-targeted delivery of antimiR-155 to *mir-155^{LSLTA}* mice using pHLIP; scale bars, 25 μ m (top, enlarged cervical lymph node) and 250 μ m (bottom, liver), $n = 3$. Red, PNA-TAMRA; blue, nucleus. **b**, Representative *mir-155^{LSLTA}* mouse before and after treatment with pHLIP-anti155, $n = 6$. **c**, **d**, Representative H&E analysis of (c) spleens and (d) livers harvested from diseased littermate

mir-155^{LSLTA} mice after treatment ($n = 6$); control spleen represents wild-type mice with no treatment. **e**, Heat map showing selected upregulated genes upon miR-155 withdrawal. **f**, Quantitative PCR (qPCR) determination of gene expression levels in lymphoid tissue from *mir-155^{LSLTA}* mice. Data are shown as mean \pm s.d., $n = 3$; statistical analysis performed with two-tailed Student's *t*-test; * $P < 0.05$; ** $P < 0.01$.

such as leukocyte transendothelial migration. We compared the upregulated genes to known and putative miR-155 targets (Supplementary Table 2) identified using the miRWalk target prediction algorithm²⁶. At the intersection of these screens, several genes are known to have tumour suppressor characteristics (Fig. 4e, Extended Data Fig. 9d and Supplementary Table 3). One notable gene is *Bach1*, a transcription factor that has been validated as a miR-155 target in renal cancer and cultured B cells^{25,27}. Gene expression analysis was used to validate *Bach1* as a miR-155 target in Toledo cells treated with pHILIP-anti155 (Extended Data Fig. 9e) and in *mir-155^{LSL/TA}* mice undergoing DOX-induced miR-155 withdrawal (Extended Data Fig. 10). Furthermore, diseased *mir-155^{LSL/TA}* mice treated with pHILIP-anti155 showed an increase in *Bach1* levels in cancerous axillary, cervical, and inguinal lymph nodes (Fig. 4f). A known miR-155 target in lymphoma, *Mafk²⁴*, was also upregulated in response to pHILIP-anti155 treatment (Fig. 4f). Therefore, pHILIP-anti155 can target lymph node neoplasms and cause effective blockage of miR-155 activity.

While oncomiRs are proving to be potent anticancer targets, in theory, using this approach, every miRNA is a 'druggable' target. Through targeted antagonism of miRNAs, pHILIP-antimiR has vast therapeutic potential for cancer and many other pathological conditions that produce localized acidic environments such as ischaemia, myocardial infarcts, stroke, tissue trauma, and sites of inflammation and infection. The main limitation of this transmembrane delivery approach involves the need for the drug cargo to have limited charge, such as PNA antimiRs. While other antimiR delivery and targeting strategies have been described^{28,29}, utilization of pHILIP to target the acidic tumour microenvironment is a widely applicable technology that will present new therapeutic and mechanistic opportunities for effective targeting of miRNA silencing.

Online Content Methods, along with any additional Extended Data display items and Source Data, are available in the online version of the paper; references unique to these sections appear only in the online paper.

Received 7 November 2013; accepted 2 October 2014.

Published online 17 November 2014.

- He, L. & Hannon, G. J. MicroRNAs: small RNAs with a big role in gene regulation. *Nature Rev. Genet.* **5**, 522–531 (2004).
- Calin, G. A. & Croce, C. M. MicroRNA signatures in human cancers. *Nature Rev. Cancer* **6**, 857–866 (2006).
- Esquela-Kerscher, A. & Slack, F. J. Oncomirs — microRNAs with a role in cancer. *Nature Rev. Cancer* **6**, 259–269 (2006).
- Medina, P. P., Nolde, M. & Slack, F. J. OncomiR addiction in an *in vivo* model of microRNA-21-induced pre-B-cell lymphoma. *Nature* **467**, 86–90 (2010).
- Babar, I. A. *et al.* Nanoparticle-based therapy in an *in vivo* microRNA-155 (miR-155)-dependent mouse model of lymphoma. *Proc. Natl Acad. Sci. USA* **109**, E1695–E1704 (2012).
- Stenvang, J., Petri, A., Lindow, M., Obad, S. & Kauppinen, S. Inhibition of microRNA function by antimiR oligonucleotides. *Silence* **3**, 1 (2012).
- Kasinski, A. L. & Slack, F. J. Epigenetics and genetics. MicroRNAs en route to the clinic: progress in validating and targeting microRNAs for cancer therapy. *Nature Rev. Cancer* **11**, 849–864 (2011).
- Cheng, C. J., Saltzman, W. M. & Slack, F. J. Canonical and non-canonical barriers facing antimiR cancer therapeutics. *Curr. Med. Chem.* **20**, 3582–3593 (2013).
- Elmen, J. *et al.* LNA-mediated microRNA silencing in non-human primates. *Nature* **452**, 896–899 (2008).
- Krutzfeldt, J. *et al.* Silencing of microRNAs *in vivo* with 'antagomirs'. *Nature* **438**, 685–689 (2005).
- White, P. J., Anastasopoulos, F., Pouton, C. W. & Boyd, B. J. Overcoming biological barriers to *in vivo* efficacy of antisense oligonucleotides. *Expert Rev. Mol. Med.* **11**, e10 (2009).
- Vaupel, P., Kallinowski, F. & Okunieff, P. Blood flow, oxygen and nutrient supply, and metabolic microenvironment of human tumors: a review. *Cancer Res.* **49**, 6449–6465 (1989).
- Reshetnyak, Y. K., Andreev, O. A., Lehnert, U. & Engelman, D. M. Translocation of molecules into cells by pH-dependent insertion of a transmembrane helix. *Proc. Natl Acad. Sci. USA* **103**, 6460–6465 (2006).
- Thevenin, D., An, M. & Engelman, D. M. pHILIP-mediated translocation of membrane impermeable molecules into cells. *Chem. Biol.* **16**, 754–762 (2009).
- Reshetnyak, Y. K. *et al.* Measuring tumor aggressiveness and targeting metastatic lesions with fluorescent pHILIP. *Mol. Imaging Biol.* **13**, 1146–1156 (2011).
- Nielsen, P. E., Egholm, M. & Buchardt, O. Peptide nucleic acid (PNA). A DNA mimic with a peptide backbone. *Bioconjug. Chem.* **5**, 3–7 (1994).
- Østergaard, H., Tachibana, C. & Winther, J. R. Monitoring disulfide bond formation in the eukaryotic cytosol. *J. Cell Biol.* **166**, 337–345 (2004).
- Rai, D., Karanti, S., Jung, I., Dahia, P. L. M. & Aguiar, R. C. T. Coordinated expression of microRNA-155 and predicted target genes in diffuse large B-cell lymphoma. *Cancer Genet. Cytogenet.* **181**, 8–15 (2008).
- Rather, M. I., Nagashri, M. N., Swamy, S. S., Gopinath, K. S. & Kumar, A. Oncogenic microRNA-155 down-regulates tumor suppressor CDC73 and promotes oral squamous cell carcinoma cell proliferation: implications for cancer therapeutics. *J. Biol. Chem.* **288**, 608–618 (2013).
- Costinean, S. *et al.* Pre-B cell proliferation and lymphoblastic leukemia/high-grade lymphoma in μ -miR155 transgenic mice. *Proc. Natl Acad. Sci. USA* **103**, 7024–7029 (2006).
- Sandhu, S. K., Croce, C. M. & Garzon, R. Micro-RNA expression and function in lymphomas. *Adv. Hematol.* **2011**, 1–12 (2011).
- Cheng, C. J. & Slack, F. J. The duality of oncomiR addiction in the maintenance and treatment of cancer. *Cancer J.* **18**, 232–237 (2012).
- DeVita, V. T., Lawrence, T. S. & Rosenberg, S. A. *DeVita, Hellman, and Rosenberg's Cancer: Principles & Practice of Oncology* 9th edn (Lippincott Williams & Wilkins, 2011).
- Zhang, Y. *et al.* LNA-mediated anti-miR-155 silencing in low-grade B-cell lymphomas. *Blood* **120**, 1678–1686 (2012).
- Gottwein, E. *et al.* A viral microRNA functions as an orthologue of cellular miR-155. *Nature* **450**, 1096–1099 (2007).
- Dweep, H., Sticht, C., Pandey, P. & Gretz, N. miRWalk-database: prediction of possible miRNA binding sites by 'walking' the genes of three genomes. *J. Biomed. Inform.* **44**, 839–847 (2011).
- Li, S. *et al.* microRNA-155 silencing inhibits proliferation and migration and induces apoptosis by upregulating BACH1 in renal cancer cells. *Mol. Med. Report* **5**, 949–954 (2012).
- Brogna, E. *et al.* Uptake by human glioma cell lines and biological effects of a peptide-nucleic acids targeting miR-221. *J. Neurooncol.* **118**, 19–28 (2014).
- Wang, Y.-Z. *et al.* Delivery of an miR155 inhibitor by anti-CD20 single-chain antibody into B cells reduces the acetylcholine receptor-specific autoantibodies and ameliorates experimental autoimmune myasthenia gravis. *Clin. Exp. Immunol.* **176**, 207–221 (2014).

Supplementary Information is available in the online version of the paper.

Acknowledgements We thank M. Bosenberg, Y. Dang, A. Karabadzhak, and J. Zhou for discussions and suggestions; R. Ardito, M. Bonk, K. Card, D. Caruso, D. Jenci, D. Laliberte, W. Nazzaro, N. Santiago, and S. Wilson for rodent services; A. Brooks for tissue pathology services; Antech Diagnostics for complete blood count analysis; E. Aronesty, B. Cooper, and E. Norris at Expression Analysis for RNA-seq services; and J. Deacon, A. Kasinski, J. Sawyer, and C. Stahlhut for reading the manuscript. C.J.C. is the recipient of a Ruth L. Kirschstein Postdoctoral Fellowship from the National Cancer Institute/National Institutes of Health (NCI/NIH) (F32CA174247). Our work has been supported by grants from the NCI/NIH (R01CA131301), the National Heart, Lung, and Blood Institute (NHLBI)/NIH (R01HL085416), the National Institute of General Medical Sciences (NIGMS)/NIH (R01GM073857), the National Institute of Environmental Health Sciences (NIEHS)/NIH (R01ES005775), the NCI/NIH (R01CA148996), the National Institute of Biomedical Imaging and Bioengineering (NIBIB)/NIH (R01EB000487), the NHLBI/NIH (2T32HL007974), and pilot grants from the Yale Comprehensive Cancer Center.

Author Contributions C.J.C., R.B., F.B., A.S., P.M.G., D.M.E., W.M.S., and F.J.S. designed the research; C.J.C. performed the research; R.B. synthesized the PNA; I.A.B. and C.J.C. developed and maintained the rodent colonies; C.J.C., Z.P., and C.L. performed the bioinformatics analysis; D.T.B. performed the pathological analysis; C.J.C., R.B., D.B., P.M.G., D.M.E., W.M.S., and F.J.S. analysed the data and wrote the paper.

Author Information Gene expression data have been deposited in the Genome Expression Omnibus under accession number GSE61851. Reprints and permissions information is available at www.nature.com/reprints. The authors declare no competing financial interests. Readers are welcome to comment on the online version of the paper. Correspondence and requests for materials should be addressed to F.J.S. (fslack@bidmc.harvard.edu).

METHODS

PNA synthesis. Regular Boc-protected PNA monomers were purchased from ASM Research Chemicals. All the given oligomers were synthesized on solid-support using standard Boc chemistry procedures³⁰. The oligomers were cleaved from the resin using *m*-cresol:thioanisole:TFMSA:TFA (1:1:2:6) cocktail solution. The resulting mixtures were precipitated with ether (three times), purified, and characterized by RP-HPLC and MALDI-TOF, respectively. All PNA stock solutions were prepared using nanopure water and the concentrations were determined at 90 °C on a Cary 3 Bio spectrophotometer using the following extinction coefficients: 13,700 M⁻¹ cm⁻¹ (A), 6,600 M⁻¹ cm⁻¹ (C), 11,700 M⁻¹ cm⁻¹ (G), and 8,600 M⁻¹ cm⁻¹ (T). The 23-base oligonucleotide PNA oligomer complementary to miR-155 has an estimated melting temperature (*T*_m) of 77.8 °C. Single-isomer 5-carboxytetramethylrhodamine (TAMRA) purchased from VWR was exclusively conjugated to the amino (N) terminus of PNAs with a hydrophilic bifunctional linker, Boc-miniPEG-3TM (11-amino-3,6,9-trioxadecanoic acid, DCHA, denoted in the sequences by -ooo-) purchased from Peptide International. Cysteine was also conjugated to the C terminus of PNAs using a Boc-miniPEG-3 linker.

The following PNA anti-miR sequences were used: anti155, TAMRA-ooo-ACC CCTATCACAAATTAGCATTAA-ooo-Cys; antiscl, TAMRA-ooo-ACCCAATC GTCAAATTCATATA-ooo-Cys; anti21, TAMRA-ooo-TCAACATCAGTCTG ATAAGCTA-ooo-Cys; anti182, TAMRA-ooo-CGGTGTGAGTCTACCATTG CAAA-ooo-Cys.

Full-length PNA anti-miRs were used throughout this study. While current technologies such as 'tiny' LNAs have seen efficacy with miRNA seed-targeted 8-base oligonucleotide anti-miRs³¹, truncated PNA anti-miRs should be similarly effective owing to their high binding affinity, which can be further enhanced with chemical modifications³².

Synthesis and characterization of pHLIP-anti-miR. To generate pHLIP-anti-miR constructs, the following pHLIP sequence (New England Peptide) was synthesized: AAQNPIYWAYADWLFTPLLLLDLALLVDADEGT(CNPys)G; conjugation of the C terminus to thiolated-PNA was facilitated by incorporating a cysteine group derivatized with 3-nitro-2-pyridinesulphenyl (NPys). To synthesize pHLIP-anti-miR constructs, pHLIP-Cys(NPys) and anti-miR PNA (peptide:PNA 1:1.3) were reacted overnight in the dark in a mixture of DMSO/DMF/0.1 mM KH₂PO₄ pH 4.5 (v/v 3:1:1) under argon. Note that this protocol was adapted from a general method of conjugating peptides to PNAs. Aside from pHLIP, attaching molecules, such as cell-penetrating peptides, to PNAs can increase cellular uptake and *in vivo* delivery efficacy^{33,34}. However, these conjugates typically require high doses and distribute to tissues throughout the body, which can result in off-target effects^{11,35}. Similarly, pHLIP can be attached to other anti-miR compositions (such as LNA), which would probably improve tumour targeting; however, physicochemical properties of PNA make them more amenable to pHLIP-mediated membrane translocation. A750-pHLIP was fabricated as previously described¹⁵.

Purification and verification of pHLIP-anti-miR. After conjugation, pHLIP-anti-miR was purified by RP-HPLC (Shimadzu) using a C18 column and a mobile phase gradient of water and acetonitrile with 0.1% trifluoroacetic acid. Purified pHLIP-anti-miR was further characterized using matrix-assisted laser desorption/ionization-time of flight (MALDI-TOF). Concentrations of pHLIP-anti-miR were determined on a Nanodrop Spectrophotometer (Thermo Scientific) at 260 nm corrected for peptide and TAMRA absorbance. Gelshift analysis used a 20% TBE gel and Bolt electrophoresis system (Life Technologies); before loading, samples were incubated with an equimolar amount of miR-155, denatured at 95 °C for 2 min, and allowed to anneal at 37 °C for 30 min. SYBR Gold (Life Technologies) was used to visualize miR-155; pHLIP and free PNA were not detected by the stain. Tricine SDS-PAGE used a 16% tricine gel (Life Technologies) and standard SDS-PAGE procedures. Samples were visualized first using TAMRA fluorescence on a Maestro 2 Multispectral Imaging System (PerkinElmer), and then using Simply Blue Coomassie stain (Life Technologies). For disulphide reduction studies, pHLIP-anti-miR was reduced for 30 min in 200 mM DTT for HPLC and EMSA, and 5 mM TCEP for tricine SDS-PAGE. For all *in vitro* and *in vivo* studies, pHLIP-anti-miR was heated at 65 °C for 10 min to prevent aggregation.

Animals. All mice were maintained at Yale University in accordance with Yale Animal Resource Center and the Institutional Animal Care and Use Committee guidelines. The *mir-155*^{LSLTA} mice were generated as previously described². For transplant studies, 5- to 6-week-old female CrTac:Ncr-Foxn1 nude mice (Taconic) were used. For toxicology studies, 8- to 9-week-old female C57BL/6J mice (Jackson) were used. For treatment of *mir-155*^{LSLTA} mice, a sample size of at least four was appropriate on the basis of *post hoc* power analysis using quantitation of spleen size (Extended Data Fig. 8d) with a 95% confidence interval. For all animal studies, group allocations were randomized and all pathological analyses were blinded to treatment groups and expected experimental outcomes.

Cell culture. For all pH-controlled cell culture experiments, cells (previously tested for mycoplasma and supplied from ATCC) were incubated with 10% FBS in RPMI

buffered at pH 7.4 with HEPES or pH 6.2 with MES, and treated with pHLIP-anti-miR suspended in reaction buffer which constituted no more than 1% of the final volume.

Histology and other techniques. Harvested tissues were fixed in 10% formalin and processed by Yale Pathology Tissue Services for H&E and terminal deoxynucleotidyl-transferase-mediated dUTP nick end labelling (TUNEL) staining. Retro-orbitally collected whole blood preserved in EDTA or serum separated using lithium heparin was sent to Antech Diagnostics for complete blood count or clinical chemistry analyses, respectively. Image quantification used ImageJ version 1.47 (NIH) and Colour Deconvolution plugin (A. C. Ruifrok). Intravital and *ex vivo* fluorescence imaging was performed on either an IVIS Spectrum System (Caliper) or Maestro 2 Multispectral Imaging System using near-infrared or TAMRA filter sets. Live mice were anaesthetized using isoflurane during image acquisition. For whole-organ studies, organs were harvested and fixed in 10% formalin before imaging.

Flank tumour establishment. To establish *mir-155*^{LSLTA} lymphoma subcutaneous flank tumours, first enlarged spleens were extracted from 2- to 3-month-old *mir-155*^{LSLTA} mice with obvious lymphadenopathy (which generally correlated with incidence of splenomegaly). Using a 100 μm pore-size cell strainer technique, spleen tissue was dispersed into a single cell suspension in 5% FBS in PBS on ice. Red blood cells were lysed using ammonium chloride lysis buffer (Stem Cell Technologies), and 5 × 10⁶ cells were subcutaneously injected into nude mice. Tumours were generally palpable within 10 days; tumour volume was calculated as (length × width²)/2.

For bioluminescent xenograft tumours, KB cells were stably transfected with firefly luciferase and clonally selected via hygromycin B selection; 5 × 10⁶ cells were subcutaneously injected into nude mice to establish tumours. Rediject D-Luciferin Ultra Bioluminescent Substrate (PerkinElmer) was administered via the manufacturer's protocol for intravital monitoring of tumour bioluminescence using IVIS Spectrum (Caliper). It was pre-established that, for all flank tumour studies, animals were excluded if their tumours had not reached a volume of 50–100 cm³ by the time of treatment. Animals were randomized into experimental arms by minimizing the differences in mean tumour size and standard deviation.

Confocal imaging and flow cytometry. For fixed cell confocal preparation, after treatment for 1 h at with 5 μM of pHLIP-anti155 (Fig. 2a), cells were washed with 1% BSA in PBS, fixed in 4% paraformaldehyde, and permeabilized using 0.1% Triton X-100 in PBS. All washes were performed using PBS at pH 7.4 to wash away surface-bound pHLIP. Actin and nuclei were stained with Texas Red-X phalloidin (Life Technologies) and Hoechst 33342 (Life Technologies), respectively. Cells were mounted in Slow Fade Gold (Invitrogen). Alternatively, Toledo cells were treated with 500 nM pHLIP-anti155 (Extended Data Fig. 2e), washed with 1% BSA in PBS, and imaged live without fixation or permeabilization. For tumour and liver tissues, organs were harvested and fixed in 10% formalin, then incubated overnight in 30% sucrose in PBS. Tumours were flash frozen in OCT before being sliced into 10 μm sections, permeabilized, stained, and mounted in Vectashield (Vector Labs). Cell and tissue confocal imaging used a TCS SP5 Spectral Confocal Microscope (Leica); confocal projections were constructed using LAS AF software (Leica) with 0.9-μm-stack height. For live cell flow cytometry, after 48 h of treatment, cells were washed five times with 1% BSA in PBS on ice and then analysed on a FACScan (BD Biosciences) using FlowJo software (Tree Star); for B220 studies, freshly harvested spleen cells (see section on Flank tumour establishment) were blocked with 10% FBS (20 min), stained with Alexa488-anti-CD45R/B220 (BD clone RA3-6B2, 20 min incubation at room temperature at 1 μg ml⁻¹ concentration), washed three times with PBS on ice, and transferred to 1% BSA 0.1% Na₂S₂O₃ in PBS on ice before analysis.

Luciferase reporter and cell viability. For dual luciferase reporter experiments, the miRNA sensor was generated by inserting the target sequence for miR-155 into the 3' untranslated region of *Renilla* luciferase on a psiCHECK-2 vector (Promega). KB cells were stably transfected using Lipofectamine 2000 (Life Technologies) and co-transfection with a Linear Hygromycin Marker (Clontech) followed by clonal selection. Utilization of stable clones was more reliable than transiently transfected cells for anti-miR studies. Cell lysates were measured for luciferase activity 48 h after treatment using the Dual-Luciferase Reporter Assay System (Promega). Control LNA anti-miR-155 (Exiqon) was delivered by lipofectamine RNAiMAX. Optimal sensor activity was seen at a 500 nM dose, although inhibition of miR-155 was also observed at lower doses. For analysis of miR-21 inhibition A549 cells were similarly treated with pHLIP-anti21 and relevant controls; however, the cells were instead transfected with a miR-21-specific LightSwitch miRNA Target GoClone Luciferase Reporter (Active Motif). Cell viability was measured 96 h after treatment using CellTiter-Glo (Promega). For both luciferase and viability assays, all treatments were performed at the indicated pH for 24 h, then media was replaced with 10% FBS in RPMI at physiological pH for extended incubation.

qPCR. For qPCR analysis of tissue after treatment with two 2 mg kg⁻¹ injections of pHLIP-anti155 or pHLIP-antiscl spaced 48 h apart, tissues were harvested 24 h after the last injection and divided into at least five representative 1 mg slices. Tissue slices were pooled into Trizol (Life Technologies) and homogenized using a Precellys 24

Homogenizer. As per the manufacturer's protocol, chloroform was added to facilitate phase separation, and the RNA-containing aqueous phase was collected. An equal volume of 200 proof ethanol was added, and RNA was purified from this mixture using RNeasy kit (Qiagen) and standard procedures with on-column DNase I digestion; standard RNeasy purification was followed for RNA extraction from cells. Reverse transcription PCR was performed with 1 µg total RNA and poly-A based iScript cDNA Synthesis Kit (Bio-Rad). Real-time PCR was performed with Quantitect Primer Assays (Qiagen) and iQ SYBR Green Supermix (Bio-Rad) using a Roche LightCycler 480 System; all samples were normalized to β-actin.

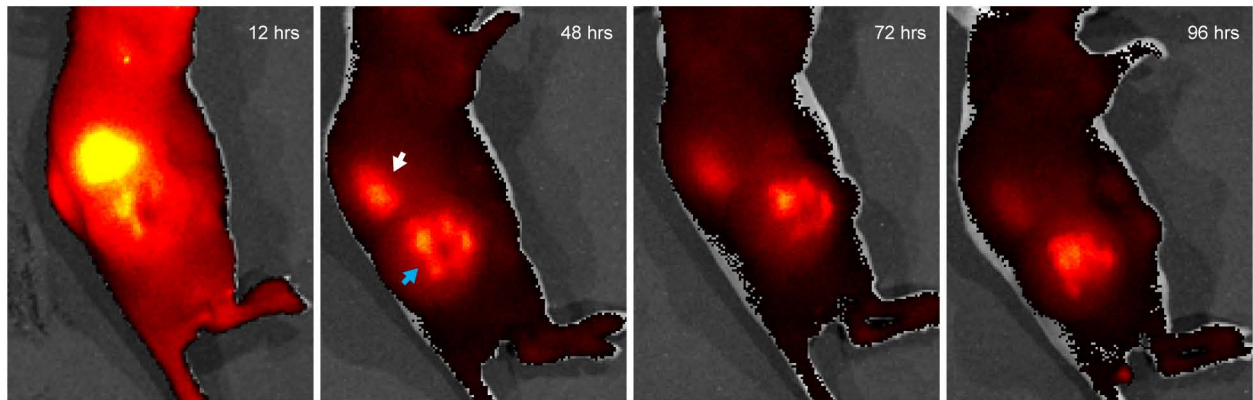
RNA-seq. For RNA-seq analysis, the overexpression and withdrawal groups both consisted of three mice with subcutaneous tumours that were established from enlarged spleens of diseased donor *mir-155^{LSLTA}* mice (Extended Data Fig. 9a). The overexpression and withdrawal mice were paired such that each of the three pairs was from a separate donor littermate. Tissue was harvested once tumours reached a volume of 1 cm³; for mice in the miR-155 withdrawal group, DOX was administered for 16 h before tissue collection. As described in the transplant methods, tumour tissue was dispersed into a single cell suspension and red blood cells were lysed. Total RNA was extracted from the remaining cells using the hybrid Trizol and RNeasy protocol described in the qPCR methods. High-quality total RNA (Agilent 2100 Bioanalyzer RIN value greater than 7) was sent to Expression Analysis for library preparation, Illumina TruSeq mRNA sequencing (50-base-pair paired end, 25 million reads per sample), alignment to the mouse genome (greater than 80% aligned to the NCBI37/mm9 assembly), and counts of the number of gene-mapped fragments given the maximum likelihood abundances. DESeq was used first to estimate size factors (that is, normalize samples by their respective sizes) and dispersions (that is, variance between samples), and then to identify differentially expressed genes

(Supplementary Table 1). Heat maps were generated using variance stabilizing transformations of the count data on the basis of a parametric fit to the overall mean dispersions.

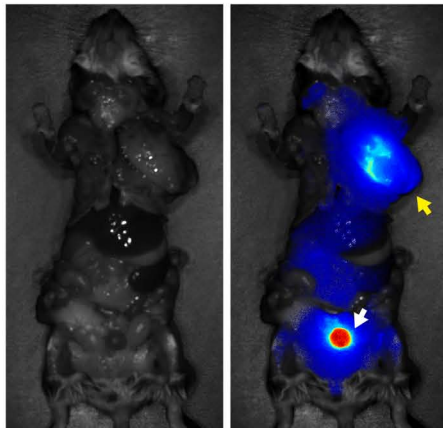
KEGG analysis. The Database for Annotation, Visualization and Integrated Discovery (DAVID, <http://david.abcc.ncifcrf.gov>) was used to identify the KEGG pathways that were enriched in the genes and both upregulated in response to miR-155 withdrawal and having a false discovery rate less than 0.05. Enriched KEGG pathways had a minimum count threshold of 2 and a modified Fisher's exact *P* value for gene enrichment less than 0.05.

30. Christensen, L. *et al.* Solid-phase synthesis of peptide nucleic acids. *J. Pept. Sci.* **1**, 175–183 (1995).
31. Obad, S. *et al.* Silencing of microRNA families by seed-targeting tiny LNAs. *Nature Genet.* **43**, 371–378 (2011).
32. Sahu, B. *et al.* Synthesis and characterization of conformationally preorganized, (R)-diethylene glycol-containing γ-peptide nucleic acids with superior hybridization properties and water solubility. *J. Org. Chem.* **76**, 5614–5627 (2011).
33. Fabbri, M. M. *et al.* Efficient inhibition of miR-155 function in vivo by peptide nucleic acids. *Nucleic Acids Res.* **38**, 4466–4475 (2010).
34. Shiraishi, T. & Nielsen, P. E. Peptide nucleic acid (PNA) cell penetrating peptide (CPP) conjugates as carriers for cellular delivery of antisense oligomers. *Artif. DNA PNA XNA* **2**, 90–99 (2011).
35. Fabbri, E. *et al.* miRNA therapeutics: delivery and biological activity of peptide nucleic acids targeting miRNAs. *Epigenomics* **3**, 733–745 (2011).
36. Xu, G. *et al.* Transcriptome and targetome analysis in MIR155 expressing cells using RNA-seq. *RNA* **16**, 1610–1622 (2010).
37. Loeb, G. B. *et al.* Transcriptome-wide miR-155 binding map reveals widespread noncanonical microRNA targeting. *Mol. Cell* **48**, 760–770 (2012).

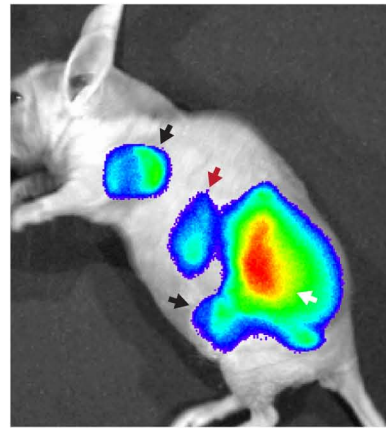
a



b

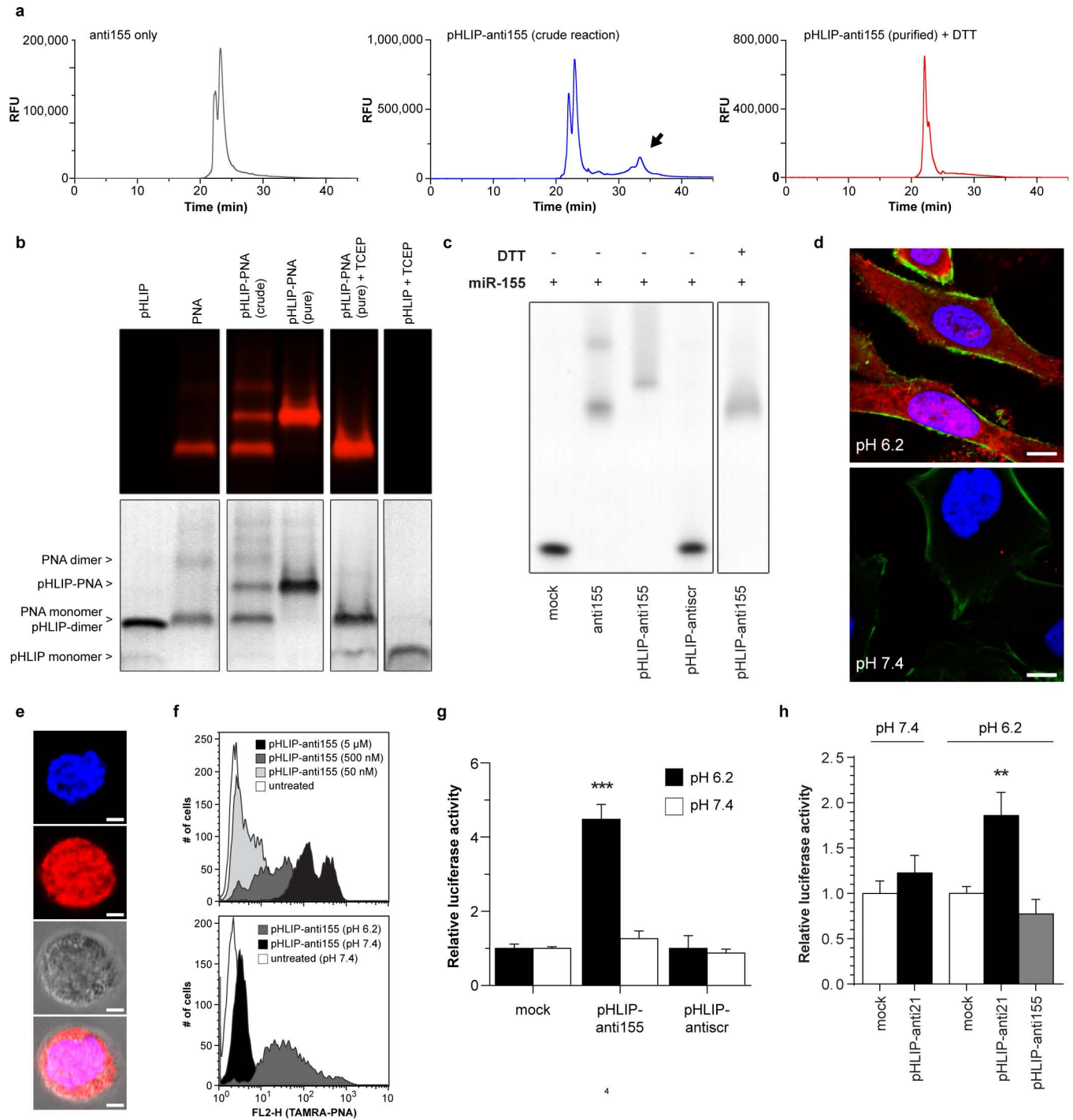


c



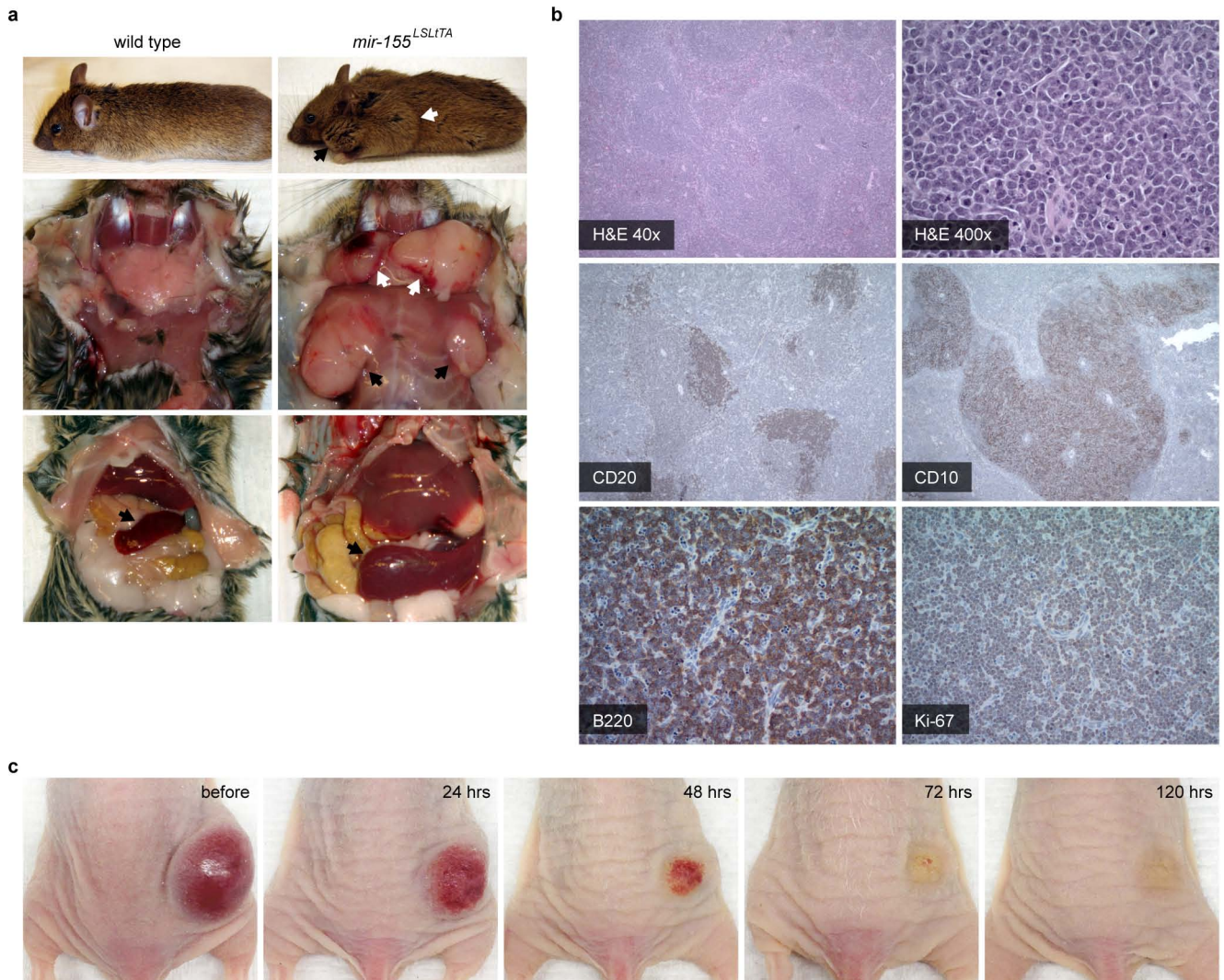
Extended Data Figure 1 | Distribution of pHLIP to the renal system and lymph node metastases. **a**, Intravenous injection of A750-pHLIP distributes to the (white arrow) kidneys and (blue arrow) tumour in a representative *mir-155^{LSLTA}* subcutaneous flank model ($n = 3$); time points indicate hours after a single injection of A750-pHLIP. Previous reports have observed systemic distribution of pHLIP to kidneys in other mouse models¹⁵. Similarly, we speculate that the increased uptake of pHLIP peptide in the kidneys is due to excretion and increased acidity of renal tubule cells. Initially kidneys are highly enriched for pHLIP, which is gradually excreted while pHLIP shows a more steady accumulation in the tumour. **b**, Representative example showing

A750-pHLIP distribution to the (white arrow) bladder and (yellow arrow) enlarged axillary lymph node 36 h after intravenous administration into *mir-155^{LSLTA}* mice with lymphadenopathy ($n = 3$). **c**, In addition to distributing to the (white arrow) primary *mir-155^{LSLTA}* flank tumour and (red arrow) kidneys, A750-pHLIP distributes to (black arrows) enlarged lymph nodes that resulted from metastatic spread; intravital fluorescence of A750-pHLIP was detected 48 h after intravenous injection into nude transplant mice with conspicuous lymphadenopathy (a representative animal from $n = 3$ is shown).



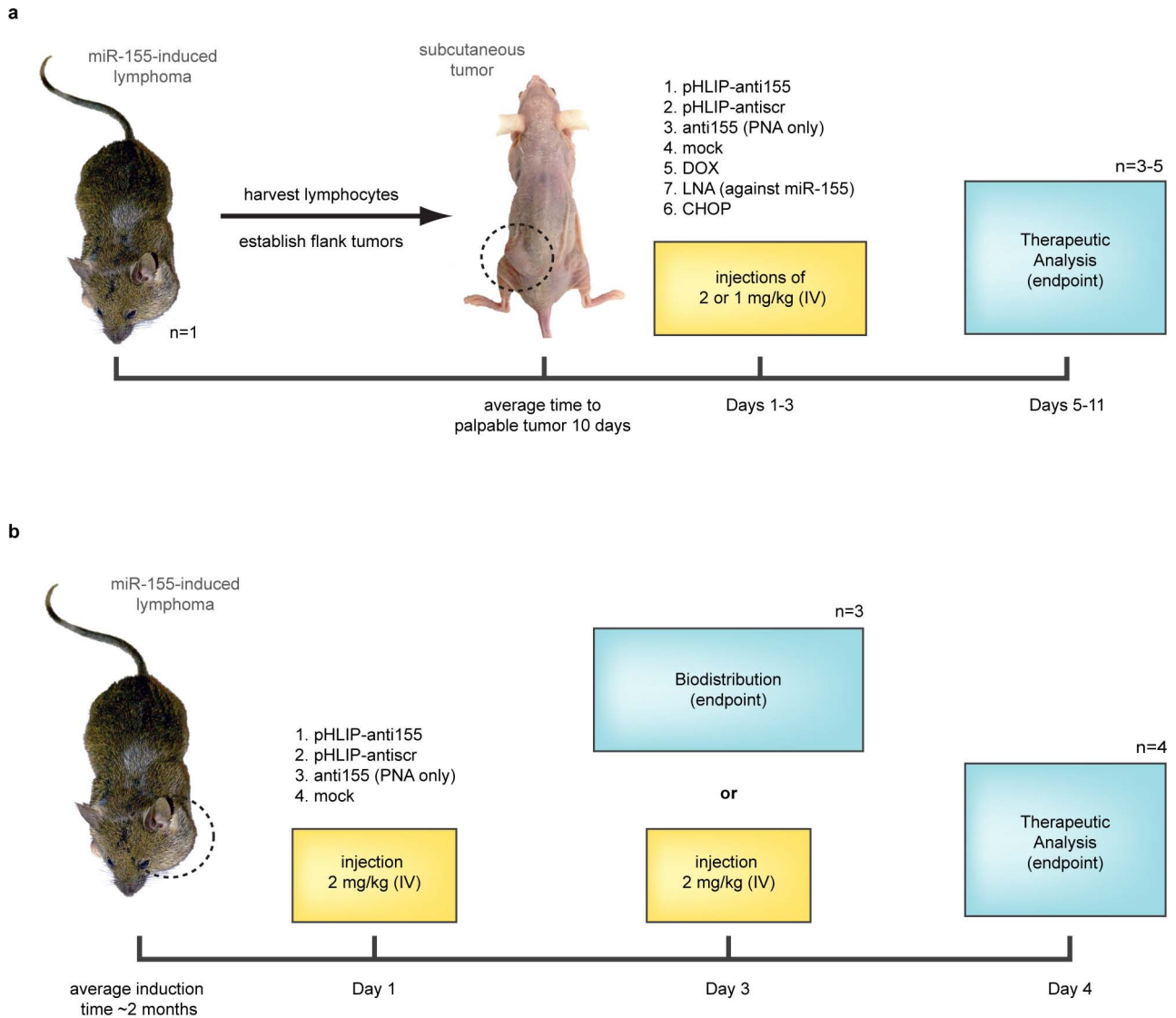
Extended Data Figure 2 | Assessment of pHLIP-PNA conjugation and activity. **a**, HPLC elution profiles of (top) free PNA, (middle) reaction mixture of PNA and pHLIP-C(Npys), and (bottom) purified pHLIP-PNA incubated in DTT. HPLC was used to purify pHLIP-PNA (black arrow). The fluorescence detection of TAMRA (ex/em: 540/575) that was conjugated to the PNA is shown; samples were also detected by absorbance at 260 and 280 nm (data not shown). **b**, Tricine SDS-PAGE evaluation of pHLIP-PNA conjugation. Gel was visualized by (top) TAMRA fluorescence to detect labelled PNA and (bottom) Coomassie stain to detect both PNA and peptide. **c**, Gelshift analysis of pHLIP-anti-miR-155 binding to miR-155 and disulphide reduction in the presence of DTT. **d**, High-magnification confocal projections of A549 cells incubated with labelled pHLIP-anti-miR (against control miR-182); scale bars, 7.5 μm . The diffuse intracellular fluorescence is indicative of freely distributed

anti-miR throughout the cytosol—note that the presence of marginal punctate fluorescence at both pH levels suggests that endocytosis is probably an additional mode of cell entry. **e**, Toledo DLBCL lymphocytes were incubated with labelled pHLIP-anti155 at pH 6.2; fluorescence of a representative live cell is overlaid on a bright field micrograph; scale bars, 2 μm . **f**, Flow cytometry analysis of Toledo cells incubated with labelled pHLIP-anti155; cell association was dependent on dose (top, pH 6.2) and pH (bottom, 500 nM dose). **g**, Inhibition of miR-155 demonstrated by de-repression of a miR-155 dual luciferase sensor in KB cells. **h**, Inhibition of miR-21 demonstrated by de-suppression of luciferase expression in A549 cells transfected with a *Renilla* luciferase sensor. Data are shown as mean \pm s.d., with $n = 3$; statistical analysis performed with two-tailed Student's *t*-test; ** $P < 0.01$, *** $P < 0.001$.



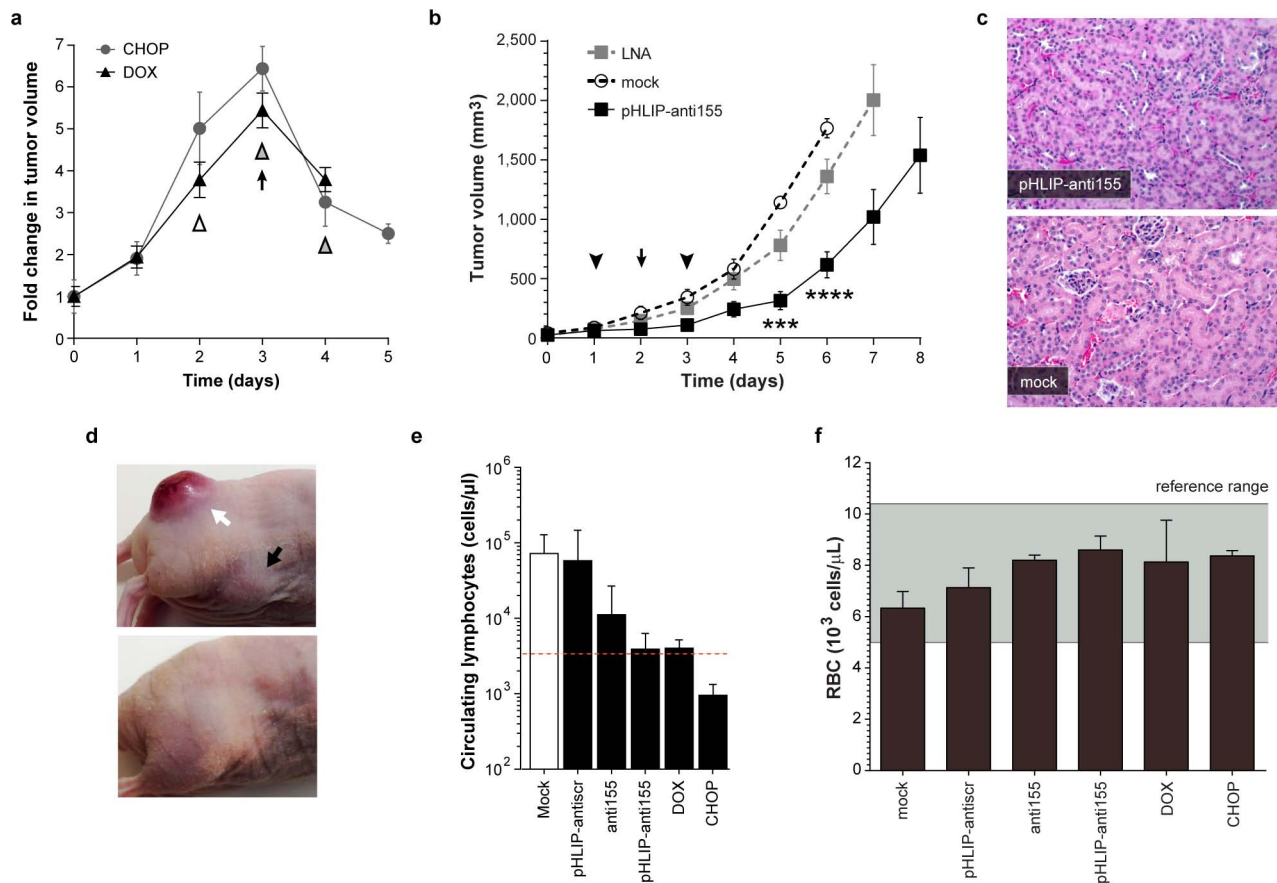
Extended Data Figure 3 | Pathology of the *mir-155^{LSLITa}* model of oncomiR addiction. **a**, Organomegaly in representative diseased *mir-155^{LSLITa}* mice: top, conspicuous lymphadenopathy seen in the (black arrow) cervical and (white arrow) brachial lymph nodes; middle, enlarged exposed (white arrows) cervical and (black arrows) axillary lymph nodes; bottom, enlarged (black arrows) spleen. **b**, Histopathology of *mir-155^{LSLITa}* mice: H&E stain of an enlarged spleen shows expansion of the white pulp by a nodular, neoplastic infiltrate; staining of the spleen shows CD20⁺ and CD10⁺ B cells of follicular centre origin. Analysis of enlarged lymph nodes indicates DLBCL with lymph

node architecture effaced by a confluent population of B220⁺ neoplastic lymphocytes and a Ki-67 proliferative index at nearly 100%; $n = 5$. **c**, Tumour regression due to DOX-induced miR-155 withdrawal in a subcutaneous tumour model established from transplanted splenic *mir-155^{LSLITa}* lymphocytes; time points indicate hours after initial administration of DOX. With a cancer phenotype that is relevant to human disease yet can be modulated by miRNA silencing, this is an excellent model for evaluating miR-155-targeted therapies.



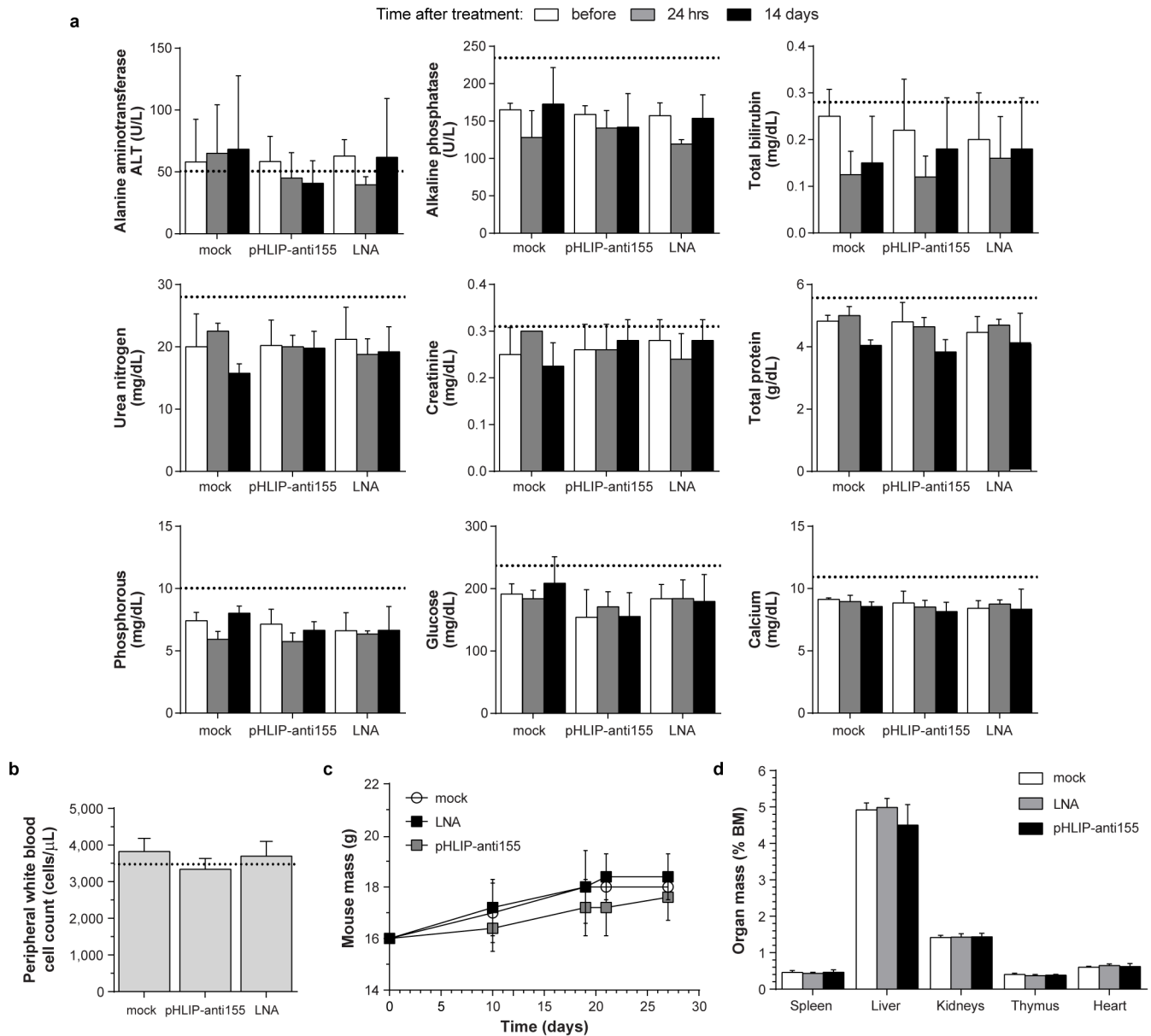
Extended Data Figure 4 | Experimental schematics for mouse tumour studies. **a**, Workflow for treatment of the *mir-155^{LSLTA}* subcutaneous flank model for the early endpoint and survival studies; day 1 indicates time of first injection. For the 'early treatment' experiments in Fig. 3a, b, d-f, h and Extended Data Fig. 5b, c, mice were treated on days 1 and 2 with pHLIP-anti155, mock buffer, pHLIP-antiscr and anti155 only; fed DOX starting on day 3; or treated with CHOP regimen on days 2-4. For survival experiments in Fig. 3c, g and Extended Data Fig. 5a, mice were treated on days

1-3 with pHLIP-anti155, LNA against miR-155, and mock buffer. **b**, Workflow for investigation of the *mir-155^{LSLTA}* model of lymphoma for the biodistribution and miR-155 silencing studies. For experiments in Fig. 4a and Extended Data Fig. 8a, b, mice were treated on day 1 with pHLIP-anti155, anti155 only, and mock buffer. For experiments in Fig. 4b-d, h and Extended Data Fig. 8c-g, mice were treated on day 1 and day 3 with pHLIP-anti155, pHLIP-antiscr, and mock buffer, or fed DOX 16 h before harvest.



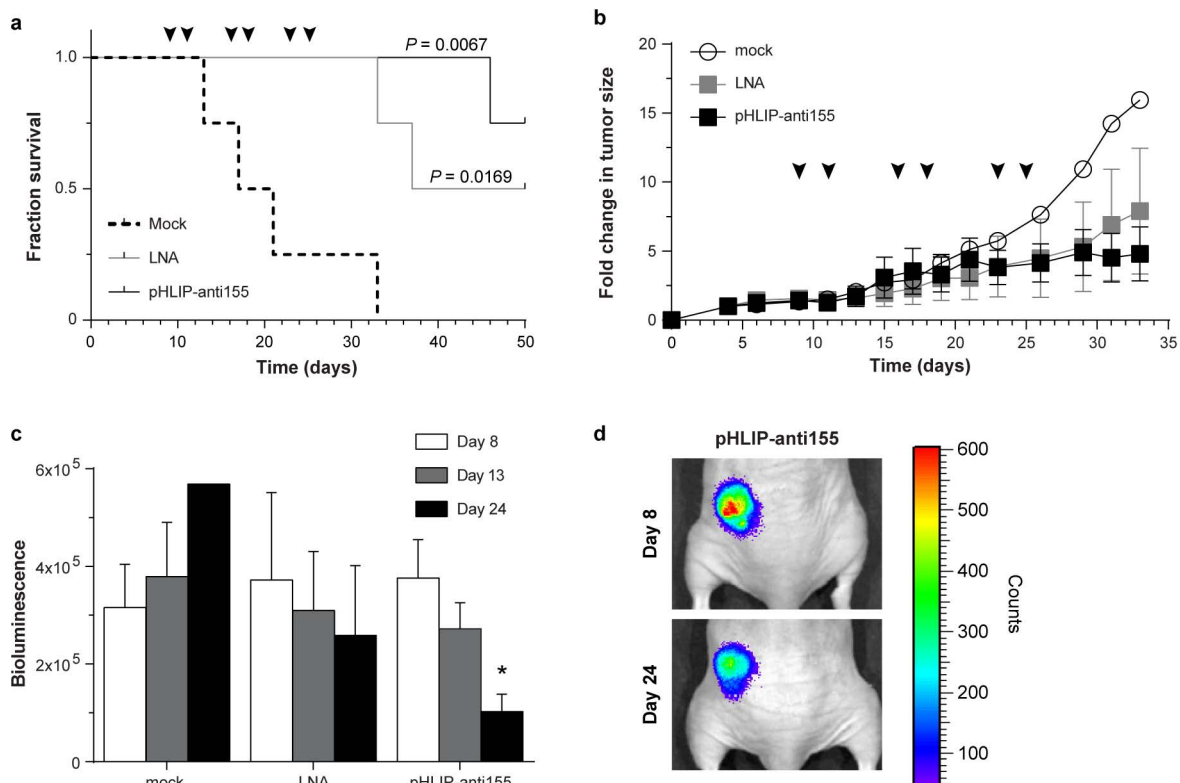
Extended Data Figure 5 | Administration of pHLIP-anti155 to mice with subcutaneous lymphoma flank tumours. **a**, Fold change in tumour size in response to miR-155 withdrawal and CHOP treatment ($n = 3$); arrow represents initiation of DOX treatment ($n = 3$, food pellets enriched with DOX at 2.3 g/kg, Bio-Serv), white triangle represents CHOP treatment (systemic injection of cyclophosphamide at 40 mg/kg, doxorubicin at 3.3 mg/kg, and vincristine at 0.5 mg/kg; oral gavage of prednisone at 0.2 mg/kg), grey triangles represent maintenance administration of prednisone. **b**, Tumour growth response to systemically administered anti-miR treatment; symbols represent intravenous injections of 2 (arrowhead) or 1 (arrow) mg kg⁻¹ of pHLIP-conjugated anti-miR-155, molar equivalent of phosphorothioated anti-miR-155 LNA, or mock delivery solution; $n = 5$, data are shown as mean \pm s.e.m.; statistical comparison of pHLIP-anti155 to LNA performed with two-way ANOVA; *** $P < 0.001$, **** $P < 0.0001$. **c**, Representative histological analysis of kidneys (H&E, $\times 100$ magnification) harvested from early endpoint

study, in which all of the mice from Fig. 3a and Extended Data Fig. 5a were killed at the same time for analysis. Kidney sections reveal an absence of microscopic changes in treated animals (pHLIP-anti155) that would be indicative of renal toxicity (compare with normal renal sections in mock control). **d**, Representative pHLIP-antisctr-treated mouse (top) with primary flank tumour (white arrow) and enlarged inguinal lymph node (black arrow) compared with an untreated mouse with no tumour (bottom). **e**, Measurement of circulating lymphocytes in blood collected at time of death in early endpoint study; dotted line denotes average level in nude mice with no tumour. **f**, Although pHLIP interacts with the outer leaflet of lipid membranes, no significant change in red blood cell (RBC) levels was detected after intravenous treatment of mice with subcutaneous *mir-155*^{LSL1TA} transplant tumours. This supports the specificity of pHLIP treatments on cells of tumour origin since pHLIP-anti-miR treatments affect the levels of circulating lymphocytes (Extended Data Fig. 5e); data are shown as mean \pm s.d.



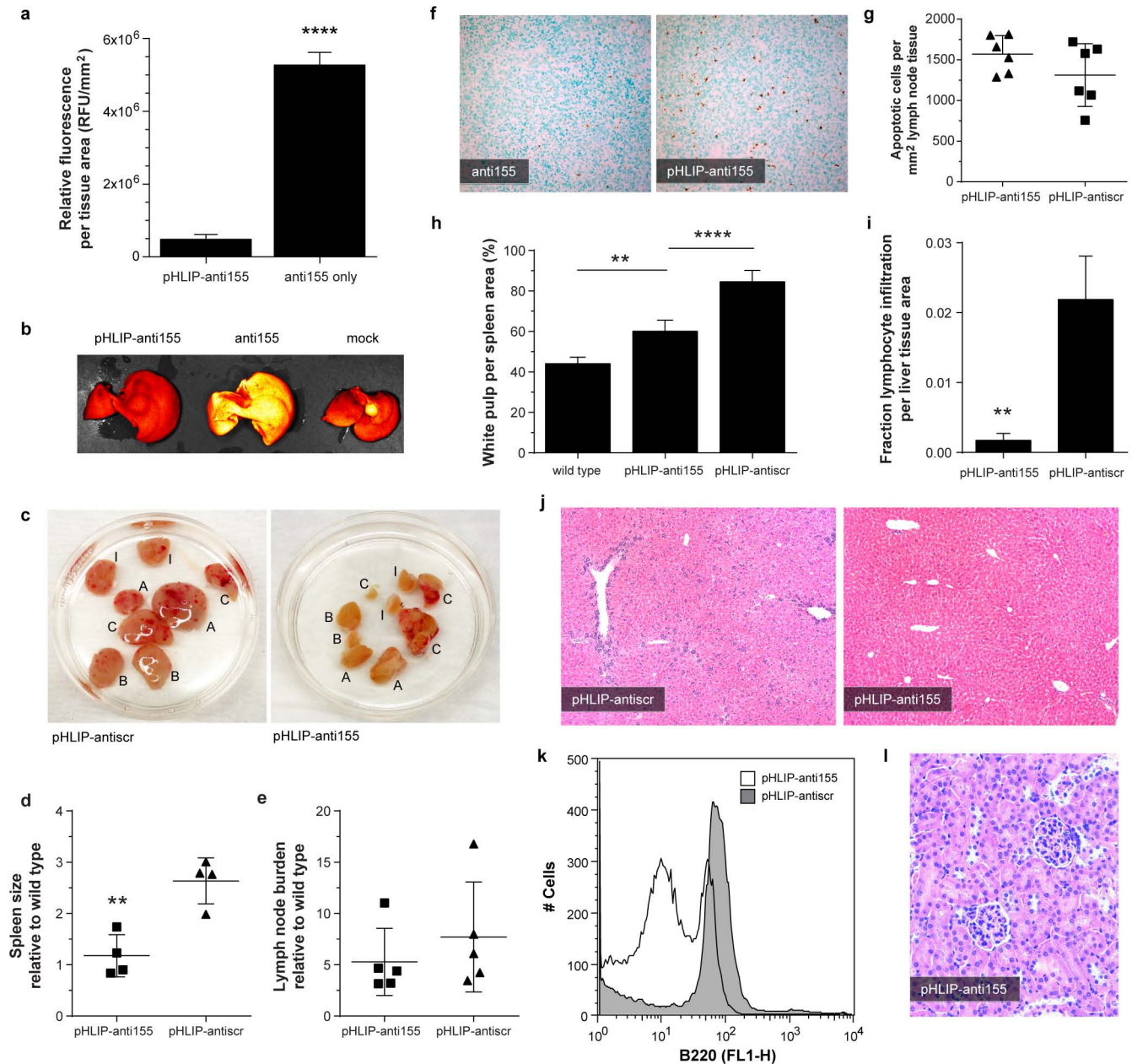
Extended Data Figure 6 | Toxicology assessment of intravenously administered pHLIP-anti155 to C57BL/6J mice. **a**, Serum-based clinical chemistry evaluation of systemic toxicity with focus on liver and kidney function; dosing schedule consisted of injections of 2 mg kg^{-1} of pHLIP-anti155 (and equimolar dose of LNA) on days 10 and 12, as well as 1 mg kg^{-1} on day 11. Blood samples were serially harvested retro-orbitally on day 0

(10 days before start of treatment), as well as 1 day and 14 days after treatment. **b**, Circulating white blood cell count collected 14 days after treatment. **c**, Mouse mass throughout duration of the study. **d**, Organ mass normalized to total body mass at time of harvest. **a–d**, For all analyses mock $n = 4$, pHLIP-anti155 $n = 5$, and LNA $n = 5$; dotted lines indicate typical wild-type values for C57BL/6J mice.



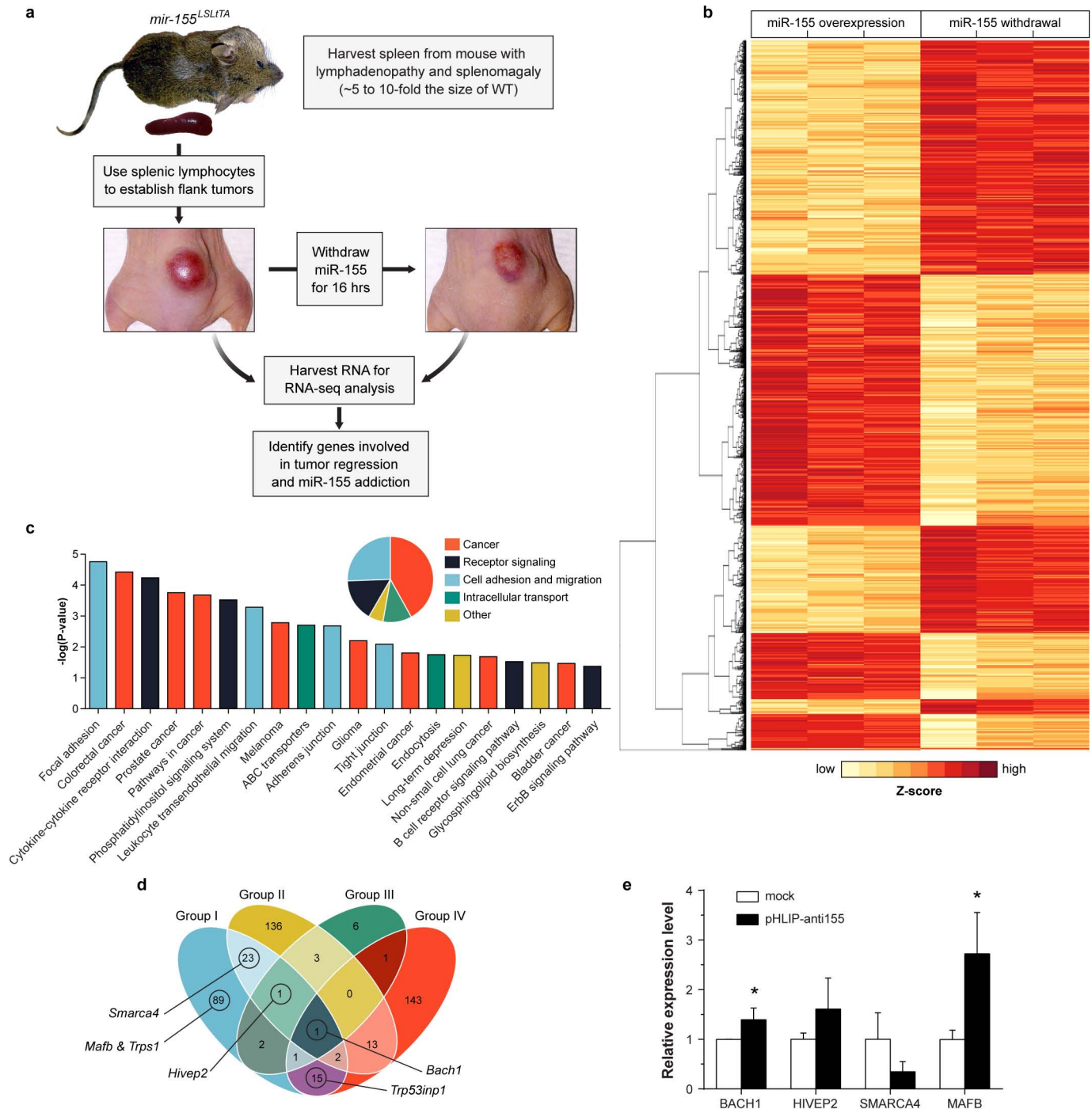
Extended Data Figure 7 | Administration of pHLIP-anti155 to mice with KB oral squamous cell carcinoma xenograft tumours. **a**, Intravenous injection of pHLIP-anti155 (***) and phosphorothioated LNA against miR-155 (*) significantly enhanced survival compared with mock buffer treatment; $n = 4$ for all groups; arrowheads indicate injections of 2 mg kg^{-1} (or molar equivalent for LNA). Survival cutoff criteria included tumour volume greater than 1 cm^3 or compassionate euthanasia, which was mandated for three

mock-treated mice with ulcerated tumours. **b**, Fold change in tumour size in response to treatment; measurements were plotted until the mock negative control group was euthanized. **c**, Tumour bioluminescence in response to treatment; day 8 represents luciferase activity before first injection. **d**, Representative images of tumour bioluminescence. Data are shown as mean \pm s.e.m.; statistical analysis performed with **(a)** Mantel-Cox analysis or **(c)** two-tailed Student's *t*-test, * $P < 0.05$; ** $P < 0.01$.



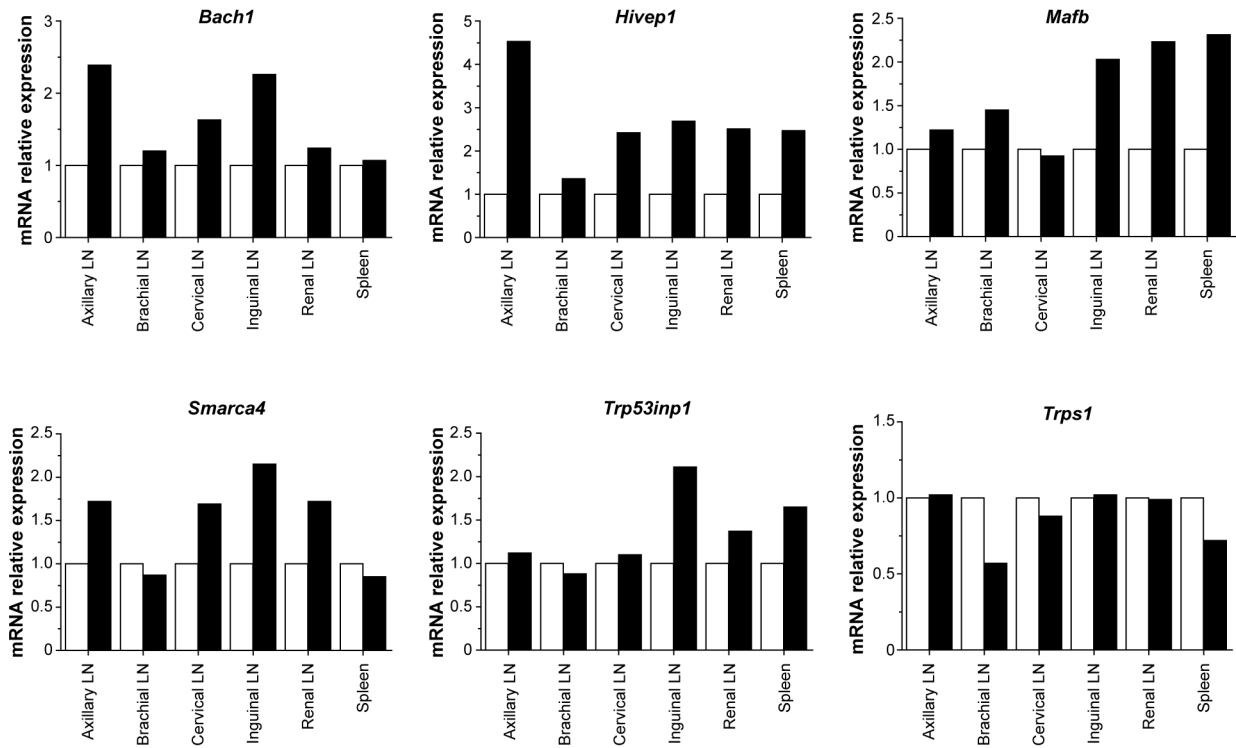
Extended Data Figure 8 | Administration of pHILIP-anti155 to *mir-155*^{LSLITTA} mice with lymphoma. **a**, Quantification of liver distribution of TAMRA-labelled PNA delivered with and without conjugation to pHILIP; ImageJ was used to measure fluorescence from five confocal sections per mouse liver; $n = 3$ mice per group. **b**, Visualization of whole liver fluorescence after anti-miR administration; pHILIP-anti155 liver fluorescence is similar to the autofluorescence seen in the mock group. **c**, Lymph-node tumour burden (A, axillary; B, brachial; C, cervical; I, inguinal lymph nodes); in these specific images taken from diseased littermates, pHILIP-antiscr-treated mice had a more than threefold larger aggregate lymph node mass (3.179 g) than pHILIP-anti155-treated mice (1.006 g). **d**, **e**, Size of harvested (**d**) spleens ($n = 4$) and (**e**) lymph nodes (axillary, brachial, cervical, and inguinal; $n = 5$) with respect to

wild type; $n < 6$ (that is, total number of treated mice) owing to size data not collected. **f**, **g**, TUNEL analysis of treated cervical lymph nodes of *mir-155*^{LSLITTA} mice ($n = 6$). **h**, Percentage of white pulp in treated spleens; $n = 6$. **i**, Measurement of lymphocyte infiltration into liver; $n = 6$. **j**, Low-magnification H&E images of livers from Fig. 4d. **k**, Flow cytometry analysis of B220-positive cells comprising the spleens of treated mice; B220 is typically a marker for B cells, although varied expression is seen on some T cells, natural killer cells, and macrophages; $n = 4$. **l**, Representative H&E image of healthy kidneys from pHILIP-anti155-treated mice; $n = 6$. Data are shown as mean \pm s.d. (**a**, **d**, **e**, **g**, **h**) or mean \pm s.e.m. (**i**); statistical analysis performed with two-tailed Student's *t*-test; ** $P < 0.01$; **** $P < 0.0001$.



Extended Data Figure 9 | Differential gene expression analysis of miR-155 withdrawal. **a**, Experimental design for RNA-seq analysis of miR-155-addicted tumours compared with tumours undergoing miR-155 withdrawal and tumour regression. **b**, RNA-seq differential gene expression analysis of three independent tumours overexpressing miR-155 compared with three independent tumours undergoing DOX-induced miR-155 withdrawal; all differentially expressed genes with a false discovery rate less than 0.05 are shown; rows are clustered by Euclidean distance measure. **c**, KEGG pathway analysis of significantly upregulated genes after miR-155 withdrawal. **d**, Selection of potential miR-155 targets involved in tumour regression. Intersection of genes (group I) that are both predicted miR-155 targets

(Supplementary Table 2) and overexpressed after miR-155 withdrawal from *mir-155^{LSLTA}* tumours (Supplementary Table 1) with genes inferred from three separate miR-155 target analyses. Group II: the study in ref. 36 used RNA-seq to compare Mutu I B cells that overexpress miR-155 with cells transformed with a control vector³⁶. Group III: ref. 25 identified shared targets between miR-155 and a viral orthologue, miR-K12-11. Group IV: the study in ref. 37 used HITS-CLIP to identify miR-155 targets without perfect seed matches in T cells. **e**, qPCR determination of gene expression levels in Toledo cells treated for 48 h with 500 nM pHLIP-anti155 at pH 6.2; data are shown as mean \pm s.d.; $n = 3$; statistical analysis performed with two-tailed Student's *t*-test, * $P < 0.05$.



Extended Data Figure 10 | Expression levels of putative targets in response to miR-155 silencing in *mir-155^{LSL1TA}* mice. qPCR validation of potential miR-155 targets involved in tumour regression using *mir-155^{LSL1TA}* mice with conspicuous lymphadenopathy treated with (black bars) DOX for 16 h

compared with (white bars) untreated mice with lymphadenopathy; all samples are normalized to β -actin; $n = 3$. Genes were selected on the basis of criteria described in Supplementary Table 3. As shown in Fig. 4f, both *Bach1* and *Mafb* have utility as biomarkers for miR-155 withdrawal-induced tumour regression.